Multigrid Calculation of Transonic Flow Past Wing-Tail-Fuselage Combinations

Arvin Shmilovich* and D. A. Caughey†
Cornell University, Ithaca, New York

A computer program for calculating transonic potential flowfields about three-dimensional wing-tail-fuselage combinations has been developed. The transonic potential equation is approximated and solved numerically using a finite volume method on a boundary-conforming coordinate system. The multigrid technique is utilized to accelerate convergence of the relaxation scheme and, thus, allow computations about multiple-component airplanes with reasonable expenditure of computer resources. The wing-tail flow interaction is investigated and results indicate that the tail exerts a noticeable effect on the wing loading when the tail is located near the wing trailing edge.

Nomenclature

a = speed of sound
$a_1, a_2, \ldots, a_7$ = coefficients of iteration matrix
b = wing span
c = section chord
C = correction to potential for current iteration
C_l, C_L = section and wing lift coefficients, respectively
C_p = pressure coefficient
d = number of space dimensions
h = determinant of Jacobian matrix
m_1, m_2 = number of smoothing sweeps when coarsening and refining grid, respectively
R = residual of Eq. (1) using solution from previous iteration
$U, V, W,$ = contravariant components of velocity
x, y, z = streamwise vertical, and spanwise coordinates, respectively
$X, Y, Z,$ = computational coordinates
δ = tail deflection angle (trailing edge down)
η = span station (percent semispan)
ρ = fluid density

Introduction

IT is of practical interest to obtain solutions for the flow past realistic airplane configurations such as wing-tail-fuselage combinations. Such computations provide insight into the nature of the flow patterns for closely coupled multiwing systems (such as fighter-type aircraft) in which the wing and tail flowfields strongly interact and the flow analyses of the individual components in isolation (e.g., wing-body and tail-body combinations) cannot be expected to be adequate for realistic modeling.

The topologies of boundary-conforming grids generally fall into three categories: 0-, C-, and H-type grids. The topologies are suggested by these letters of the alphabet. O-type grids have one coordinate surface which wraps completely around the body; the conformal mapping of an airfoil to a circle is the most common example. C-type grids have one coordinate surface which wraps around the body and a branch cut extending to infinity (which is frequently used to represent a vortex sheet). H-type grids are nearly Cartesian, with the body included within a double-valued segment of one surface; a stream-function/potential-function coordinate system is an example of this grid type.

Grids generated for wing-tail-body arrangements[1] have been used in the present work for the computation of transonic potential flow within the framework of the finite volume method. The mesh generation procedure produces a boundary-conforming grid of type C for the wing and type H for the tail. An essential advantage of the finite volume method is the decoupling of the grid generation step from the iterative procedure used to solve the flow equations. This is particularly important when the body about which the flow is to be computed is relatively complex.

Obviously, many mesh cells are needed for modeling the flow past a complete airplane to achieve adequate resolution in the vicinity of the individual components. In the present work, the multigrid technique has been used to improve the iterative convergence rate and, hence, enhance the practicality of such computations. Experience gained in two- and three-dimensional numerical calculations,[2-4] both in the programming and predictability aspects, helped greatly in developing the present program. The multigrid version of FLO-30 (known as FLO-30M[4]) formed the point of departure for developing the wing-tail-body program described herein.

In the following a description of the iterative process is provided and implications of its use with the multigrid method on a three-dimensional slotted computational domain are discussed. Numerical flow calculations demonstrating the beneficial effect of the multigrid technique in accelerating the conventional relaxation scheme are presented. The flow computation results emphasize a study of the flow pattern near the tail and the wing-tail interaction. A parametric study has been conducted to assess the effect of tail location and deflection. Throughout this paper reference is made to a companion article[1] which describes the mesh generation module for the wing-tail-body code. Additional details are contained in Refs. 5 and 6.

Analysis

The continuity equation for steady potential flow in an arbitrary coordinate system $X, Y, Z,$ reads[7]

$$(\rho h U)_X + (\rho h V)_Y + (\rho h W)_Z = 0 \qquad (1)$$

Noting that the equation representing conservation of mass is equivalent to $\rho h/a^2$ times the potential equation in quasilinear form, the latter is utilized to formulate the iterative scheme. In order to reflect the limited domain of dependence properly, a second-order artificial viscosity is in-

Received July 10, 1984; revision received Feb. 21, 1985.

*Post-Doctoral Associate, Sibley School of Mechanical and Aerospace Engineering; currently; Senior Engineer/Scientist, Douglas Aircraft Company, Long Beach, California.

†Professor, Sibley School of Mechanical and Aerospace Engineering. Associate Fellow AIAA.

troduced in hyperbolic regions of the flowfield.[4] The solution of the algebraic equations resulting from the discretization is accomplished by an iterative scheme, formulated by embedding the steady-state equation in an artificial time-dependent equation.

To be effective in conjunction with the multigrid technique, the relaxation scheme must efficiently damp the high wavenumber components of the residual. Successive line overrelaxation (SLOR) has been used in the present work. This procedure is characterized by considering one mesh line at a time, and simultaneously calculating the corrections at points that lie on it. Specificially, the discretized equations are solved sequentially in planes of constant Z (marching from the fuselage toward the lateral boundary), solving along the lines of constant X and marching in the X direction (XSLOR), or along lines of constant Y and marching in the Y direction (YSLOR). The resulting equations form a pentadiagonal, diagonally dominant system on each line.

The system of equations for the XSLOR scheme, i.e., when the corrections are calculated simultaneously along X lines (corresponding to constant indices i and k) is of the form

$$a_1 C_{i,j-2,k} + a_2 C_{i,j-1,k} + a_3 C_{i,j,k} + a_4 C_{i,j+1,k}$$

$$+ a_5 C_{i-2,j,k} + a_6 C_{i-1,j,k} + a_7 C_{i,j,k-1} = -R_{i,j,k} \qquad (2)$$

for positive components of the contravariant velocity. The expressions for the coefficients may be found in Ref. 4.

In a similar fashion it is possible to devise a scheme in which points along Y lines are updated simultaneously, marching in the Y direction (YSLOR). Both X and Y schemes have been implemented in the present program.

It was shown in Ref. 2 that the growth factor in a local mode analysis of the XSLOR scheme should never exceed 0.78 per multigrid cycle (or 0.883 per work unit for the strategy described below) if the multigrid technique is effective in reducing all low wavenumber components of the error in any of the three coordinates. However, the actual performance is not this good, presumably because errors are replenished in the course of the multigrid iteration (due to residual restriction and interpolation of corrections). Errors are most probably excited in the far-field region of the domain, particularly near the downstream boundary where the modulus of the transformation is large and the mesh cells are highly elongated. This contention has been borne out by numerical experiments with the XSLOR scheme which exhibited slow asymptotic rates of residual reduction (in many cases as slow as the nonmultigrid scheme) but showed good convergence of the solution near the lifting surfaces.[3] However, it was found effective to alternate between XSLOR and YSLOR schemes (alternating successive line overrelaxation) at each grid level within each multigrid cycle, resulting in the efficient elimination of all high wavenumber components of the error.

Implementation Aspects

Boundary Conditions

The treatment of boundary conditions in a boundary-conforming coordinate system is accomplished quite easily since the finite difference scheme is formulated in terms of the contravariant components of the velocity vector. To enforce the no-flux condition across solid surfaces (the fuselage, wing, and tail) and the vertical plane of symmetry, the normal component of the velocity vector must be zero. This is enforced by reflecting the normal flux contributions for the cells adjacent to the boundary.

The algorithm is simplified by introducing a reduced velocity potential describing perturbations from the freestream. This potential is set to zero on the upstream and lateral far-field boundaries. On the far downstream boundary, the first derivative in the freestream direction of the perturbation potential is set to zero; this is equivalent to setting the streamwise velocity component to its freestream value. This boundary condition is a consequence of the irrotationality of the flow and the fact that the flow becomes fully developed far downstream. The manner in which this boundary condition is incorporated in conjunction with the multigrid procedure is described below.

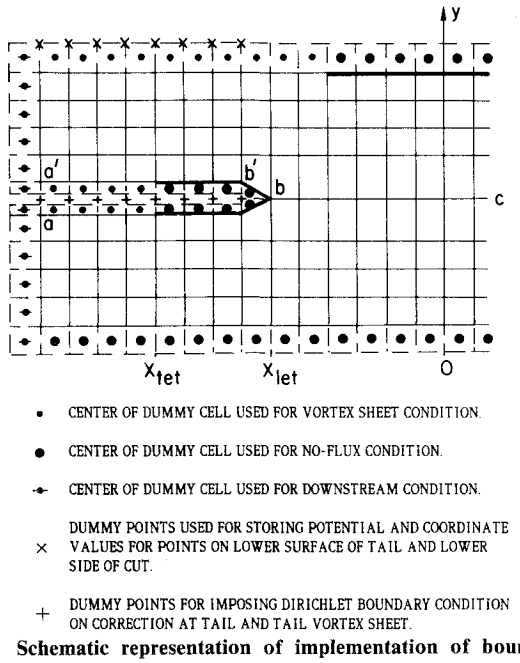

Fig. 1 Schematic representation of implementation of boundary conditions.

To account for lift, vortex sheets emanating from the trailing edges of the lifting surfaces must be allowed. It is assumed that the wing trailing vortex sheet lies in a specified surface; thus convection and roll-up are ignored. On the two sides of the sheet, conservation is required. For this purpose it is convenient to introduce dummy cells above the boundary which are identified in the physical domain with the corresponding interior cells on the other side of the cut. Points on the cut are treated as interior points by the same iterative algorithm. This procedure also can be used when the cut is a vortex sheet across which the jump in the potential is determined by the Kutta condition.

The potential values at points which lie on the tail and its associated vortex sheet are also calculated by the universal flow algorithm. This is done by introducing a dummy cell adjacent to each cell on the slit, as shown in the schematical computational plane in Fig. 1.

Slotted Computational Domain—Aspects of Computation

Coding complications are introduced by the need to relax the solution along lines intersecting the slit representing the images of the tail and its vortex sheet in (portions of) the computational space. Since the mesh line passing through the tail and its vortex sheet is double-valued, the potential and coordinates at points lying on its upper branch are stored in auxiliary locations of the respective arrays. These quantities need to be retrieved in the course of each relaxation sweep.

When using XSLOR, the number of points along a given X line depends upon whether it is upstream or downstream of the tail leading edge. In fact, an X array in the part of the domain downstream of the tail leading edge is longer than a line in the rest of the domain by two points: in addition to the mesh point needed to represent the slot boundary (the ×'s in Fig. 1), a dummy point is introduced so that for any X, the entire X line may be updated simultaneously, invoking Dirichlet boundary conditions on the artificial corrections at the dummy points (represented by pluses).

When using YSLOR, the corrections at points that lie on the line passing through the tail are computed in two steps: first, corrections are computed on the line a-b-c (assuming we march from the line $Y=0$ upward), and then the string of points a′-b′ is updated using the correction at point b (which has already been determined for the current iteration) as a Dirichlet condition.

Since the domain is swept in the outboard direction, quantities computed in the plane that passes through the tip of the tail and its outboard neighbor are used for computing the solution on the latter. While the computational tip plane is slotted, planes outboard of the tip are not. This complicates matters and special care must be taken for the correct identification of the stored quantities (from the tip plane) when the plane next to the tail is being swept.

Clearly, careful bookkeeping of indices is necessary for both XSLOR and YSLOR. To make the code efficient the proper indices of the various quantities are stored in ("integer-type") arrays which are reinitialized before each line is relaxed. This almost completely eliminates logical checks (i.e., "if" statements) inside "do" loops. This treatment is important for computational efficiency when running the program on vector computers or array processors.

The topology of the mesh system at the leading edge of the tail is somewhat different from other cells in the domain. The residual at a point on the leading edge of the tail is calculated by averaging the fluxes at 12 cell centers (10 for the tip point), of which eight are field cells and four (two at the tip) are dummy cells used to facilitate enforcing the no-flux condition. A simple calculation shows that the flux balance in the seemingly different auxiliary cell may be computed in exactly the same manner as at any ordinary cell.

The Multigrid Algorithm—Implementation Aspects

For the application of the multigrid method to the computation of three-dimensional transonic flows, the continuity equation and boundary conditions described previously are discretized on a sequence of grids. The coarse grid levels are constructed by eliminating every other mesh point in each direction.

The only disadvantage of multigrid techniques is the complex programming involved. Special programming is needed for transferring the potential and the weighted residuals to the next coarser grid, for the interpolation of the corrections to the next finer level, and for the coarsening/refining of the mesh. Separate routines were programmed for most of the steps in the multigrid process.

The transfer of the potential is done by *injection*, i.e., values of the potential from the fine grid are transferred at points corresponding to both levels.

Three fine grid planes contribute to the construction of the volume average of the residuals. Dummy points are introduced next to all boundaries of the domain (solid and free boundaries and vortex sheets) and are assigned the values of the residuals at the neighboring interior points. This permits the restriction of residuals near the boundaries to be performed by the same averaging operator as used for interior points. The restriction of residuals at the leading edge of the tail, where more points are involved, is somewhat different, as is the weighting of the residual at points lying on the tip of the tail and the edge of the vortex sheet.

A special routine was devised for transferring the corrections from coarse to fine grids. Four coarse grid planes participate in forming a four-point Lagrangian interpolation in each direction. Nonsymmetric three-point interpolation formulas are used for transferring the corrections to points adjacent to the boundaries.

A fixed strategy for changing levels has been effective in the present calculations. The domain is swept m_1 times on each grid level, except the finest, until the coarsest grid is reached. Each level is swept m_2 times after coarse grid corrections are added while backing up to the finest grid. This completes a multigrid cycle. Thus, the work required for one multigrid cycle for a problem in d space dimensions is

$$1+(1+m_1)(1/2^d+1/2^{2d}+\ldots)+m_2(1+1/2^d+1/2^{2d}+\ldots)$$
$$<[m_1+2^d(1+m_2)]/(2^d-1)\text{ units} \quad (3)$$

where one work unit is the labor required for one fine grid iteration. Since the cost of computing the residuals constitutes most of the computational effort for a relaxation sweep in the present calculations, this was also taken as the cost of calculating the residuals for restriction to the next grid level (on that grid). The strategy with $m_1=4$ and $m_2=2$ was found to be the most effective. It has been experimentally verified (by comparing actual machine computation time) that this conservative choice for gaging the work spent for the residual calculation accurately reflects the actual cost of their calculation as well as the overhead spent for the other transferring functions (of the solution and of the correction) and the coarsening/refining of the mesh.

As described previously, the incorporation of the boundary conditions on solid surfaces and on the vortex sheets allows use of the same algorithm as at internal points. This feature is particularly important when using the multigrid algorithm, since it does not introduce nonsmooth residuals at boundary points. The Dirichlet boundary conditions on the upstream and lateral boundaries also maintain the smoothness of the residuals.

Difficulty was encountered, however, when trying to impose the Neumann condition for the velocity potential on the downstream boundary (which was done in FLO-30 by setting the potential on the boundary plane to its value on the third plane upstream of the boundary). This difficulty is overcome by invoking the Neumann condition directly in the following manner: fictitious cells are introduced next to the downstream boundary; their velocities in the streamwise direction (at the center of the cells) are set such that the velocities have the required value on the boundary; the standard algorithm is then applied to calculate the potential on the downstream boundary. This approach is a generalization of that used at points on solid surfaces and the vortex sheet.

Results

The geometry tested in flow computations is the ONERA wing M-6 and a tail whose cross section is identical to the wing section, mounted upon a cylindrical body of radius equal to 0.25 times the semispan. The wing is midmounted upon the fuselage at zero incidence so that in the absence of the tail and at zero angle of attack the flow is symmetrical about the wing plane. The wing has a 30 deg leading-edge sweep, a taper ratio of 0.562, and a uniformly tapered cross section of approximately 10% thickness ratio. The chord at the root of the tail is 0.7 times the chord of the wing root section. The tail has a dihedral of 10 deg and is mounted at 0.08 semispan above the wing plane. The tail can be deflected about a nonswept pivoting axis that passes through its midchord at the root.

Two configurations were investigated, differing only in the tail planform. The first, referred to as configuration 1, has a tail planform similar to that of the wing which extends outboard to 0.52 semispan. The second, referred to as configuration 2, has a tail with a 40 deg leading-edge sweep, a taper ratio of 0.494, and a tail semispan of 0.48 times the wing semispan. Members of each configuration type are identified by the longitudinal position of the tail, i.e., by the horizontal distance from the trailing edge of the wing (stagger).

Most of the computations were carried out on a mesh of $192\times32\times24$ cells in the X, Y and Z directions, respectively, unless otherwise noted, with the crudest grid in the multigrid sequence (corresponding to the fourth level) containing $24\times4\times3$ cells. The longitudinal distribution of cells is as

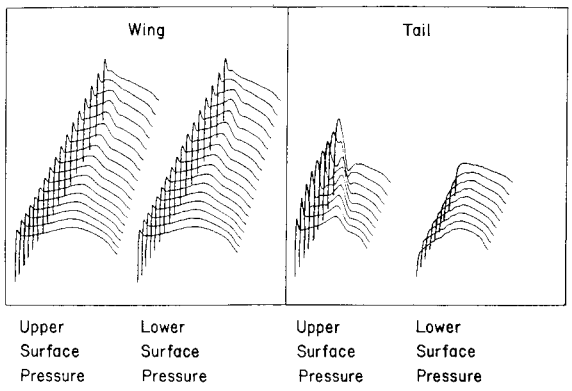

Fig. 2 Surface pressure distributions for wing and tail of the first ONERA combination ($M_\infty = 0.88$, $\alpha = 0$ deg, $\delta = +4$). Tail is located at 0.12 the wing root chord.

follows: 40 cells are put on each side of each lifting surface, 8 cells lie between the surfaces, and 8 cells lie between the tail and the downstream boundary. An equal number of cells is put between the tail and the branch cut and between the tail and the symmetry plane. In the spanwise direction, 16 cells are placed on the wing, of which one-half are also placed on the tail.

Clearly, fine grids are needed for computing the flow past wing-tail-body combinations to resolve the flow near all lifting surfaces. However, the flow computation is only about 10% more expensive per mesh point than the flow calculation in the code devised for wing-body combinations. The computational work required per mesh point for mesh generation about the tail-on configuration is less than twice as great as that for the tailless combination.[1] Overall, since the work required for mesh generation is only about one-half the work required for one iteration of the flow solver, the code for the wing-tail-body configuration is almost as efficient as the multigrid version of FLO-30. For the $192 \times 32 \times 24$ grid the code requires computational time equivalent to approximately 3.3 s of CPU time per work unit on the CRAY I computer. Using the multigrid method, solutions had converged to within engineering accuracy in the equivalent of about 30 relaxation sweeps, independent of the fineness of the mesh. The computational time required for the flow calculation on this grid would be approximately 100 s of CPU time on the CRAY 1. For all of the flow calculations performed, a well-converged solution was obtained within 50 work units (requiring 167 s of CPU time). This is consistent with the estimate of computational work required for obtaining solutions converged to the level of the truncation error as predicted in Ref. 2.

At this point it is useful to describe the general features of the flow pattern for a two-wing system. If the wing and tail are oriented such that the lift is positive on both surfaces, the wing vortex system has a downwash effect on the tail, effectively reducing its angle of attack. Hence, the lift on the tail would be lower than that produced by it in isolation. At the same time, the tail vortex system induces upwash in the upstream region outboard of the tail tip, and either a downwash or upwash inboard, depending upon the geometry. The lift on the wing can thus be greater or smaller than that produced by it in a tailless arrangement.

This vortex description is adequate if the horizontal spacing between the wing and tail is large. For closely coupled configurations, additional effects must be included. The results to be presented emphasize configurations whose tails are very close to the wing (as close as about 6% of the wing root chord). A description of the flow pattern and the interaction between the lifting surfaces for these closely coupled configurations will be given later.

In the first set of results, the performance of the iterative procedure and the benefits resulting from the use of the multigrid technique will be examined. The surface pressure distributions on each of the moderately coupled lifting surfaces of the first combination are shown in Fig. 2; the distance between the wing and tail at the root is 0.12 of wing chord. The freestream Mach number is 0.88 and the configuration is at zero angle of attack with the tail deflected +4 deg (trailing edge down). These conditions result in moderately sized supersonic zones (containing approximately 4.4% of the points on the grid used). The solution had converged to within 1% of its asymptotic values for tail lift and total number of supersonic points in about 25 work units. The effectiveness of the multigrid method has been demonstrated on even finer grids containing as many as 212,025 mesh points, with convergence to within 1% of asymptotic values of force coefficients in approximately 30 work units.[5]

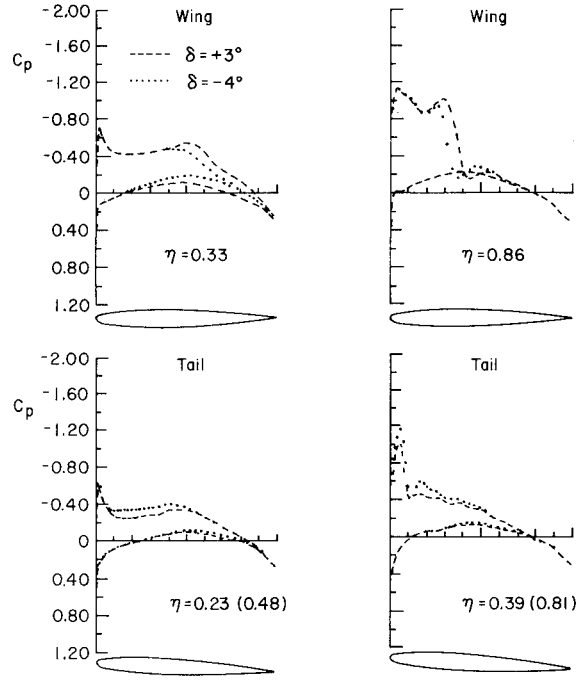

Fig. 3 Effect of tail deflection upon wing and tail surface pressures for M_∞ and $\alpha = 3.06$ deg. The tail is at a distance of 0.0625 the wing root chord.

Experiments were performed to furnish information about the wing-tail interaction for a closely coupled configuration. The ONERA combination of the second type with a stagger of 6.25% of the wing chord at the root section is considered typical. A parametric study was conducted to assess the effect of tail location and deflection. Calculations were carried out for two flow conditions. The first is a freestream Mach number of 0.84 and 3.06-deg angle of attack. Streamwise pressure distributions at two span stations for each of the lifting components are plotted in Fig. 3. These are presented for tail deflections of +3 and −4 deg. The close tail has a blockage effect on the flow near the wing upper surface and accelerates it near the lower surface. The effect of the tail (which extends to 0.48 of the wing semispan) on the wing lower surface (on which the flow is entirely subsonic) is limited to the inboard stations. Only at these stations is the tail very close to the wing's trailing edge (since the tail leading edge is swept by a larger angle than the wing trailing edge and because of the tail dihedral). On the other hand, the entire upper surface of the wing is affected by the presence of the tail. The increase in the pressure near the tail leading edge reduces the suction in the region downstream of the aft shock of the wing. This, in turn, reduces the strength of the shock which terminates the supercritical region, causing it to shift upstream. In other words, information about the presence of the tail is transmitted upstream via the sub-

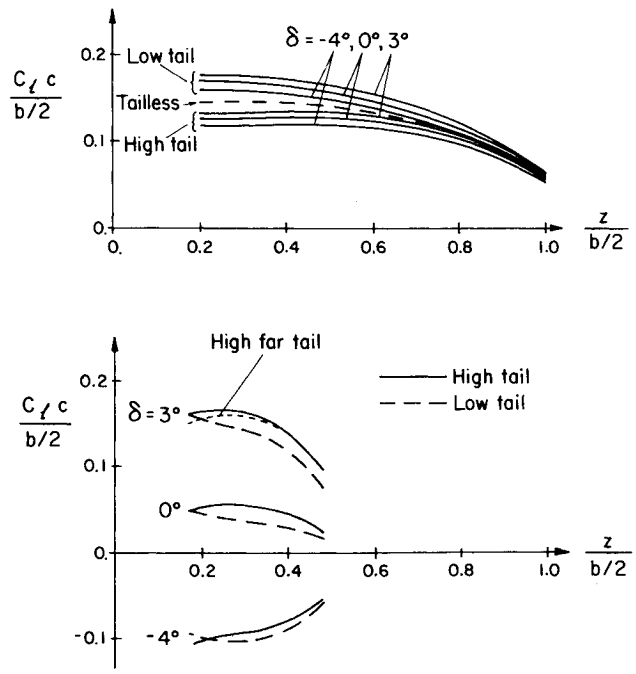

Fig. 4 Spanwise loadings on wing and tail as a function of tail deflection for the freestream condition as in Fig. 3.

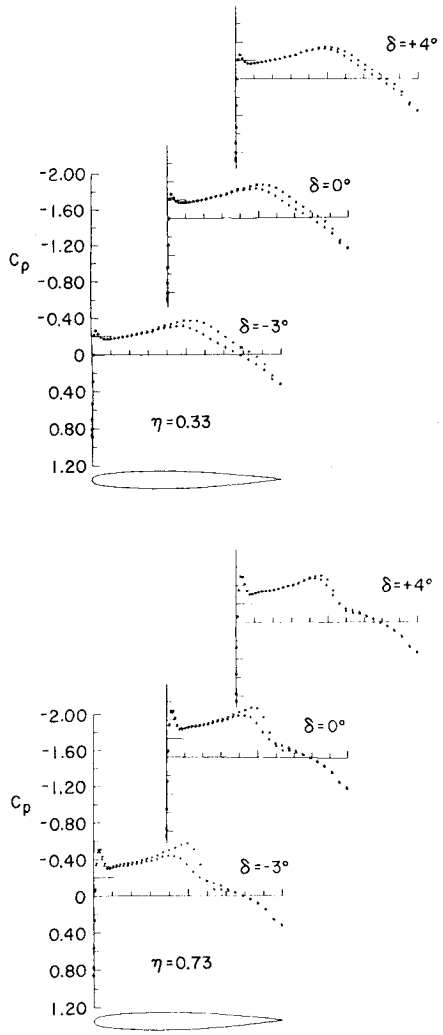

Fig. 5 Effect of tail deflection upon wing pressure distribution for $M_\infty = 0.88$ and $\alpha = 0$ deg.

critical region behind the aft shock, causing relocation of the shock. The tail effect diminishes outboard in the same way its effect on the wing lower surface becomes less pronounced at outboard stations. However, since the aft shock which extends to the tip of the wing originates (on the inboard part of the wing) further upstream than its location in the tail-off configuration, its relocation extends all the way to the tip. This can be observed in Fig. 3 where, independently of the tail deflection, the wing upper surface pressure is indistinguishable in the aft region of the section at the 0.86 spanwise station while the shock is shifted upstream.

The wing pressure distribution for the arrangement with the close tail deflected at +3 deg is not significantly different from the distribution for the tailless configuration. The effect of the tail is most prominent when the tail is deflected at −4 deg. The reasons for the difference in wing pressure as a function of tail deflection are twofold. First, the location of the leading edge of the tail with respect to the wing affects the wing upper surface pressure blockage effect: for the +3-deg deflection the leading edge is 13% higher than its vertical location in the case of the nondeflected (zero angle) tail, while for the −4-deg angle the leading edge is displaced 17% downward from its level in the no-deflection case. Hence, the closer the leading edge of the tail is to the wing, the more the flow on the upper surface of the wing is decelerated. Second, considering the closely coupled wing and tail as one aerodynamic unit, the tail deflection changes the effective camber of the wing-tail combination. Thus, the larger the negative deflection of the tail, the more the flow on the lower surface of the wing is accelerated. In a sense, for negative tail angles, the situation is similar to the flow past a wing having trailing-edge flaps deflected upward.

The presence of the tail causes a reduction in wing lift relative to the tailless configuration. Figure 4 shows the spanwise loading on the wing and tail for the three tail deflections. Both high and low tails (positioned at the same distance from the wing plan) are considered. Flow computations about low tail arrangements can be performed by the same code provided the wing and body are symmetrical about the wing plan. The low tail condition is obtained by reversing the signs of the angle of attack and the tail deflection. The considerations addressed above regarding the flow past closely coupled wing/high-tail arrangements are similarly applied to low tail combinations. In contrast to the high tail, the presence of the low tail enhances the lift of the wing, especially for large positive tail angles. For positive tail deflections, the flow pattern is similar to that past a wing with extended Fowler flaps. The departure of the wing loading for high and low tails from that in the absence of the tail is shown in Fig. 4. In the plot of the tail loading, note the load distribution on the high tail at +3 deg, positioned at 75% of the wing root chord behind the wing. Near the tip there is no significant difference in the loading because even for the near tail the gap between the trailing edge of the wing and the leading edge of the tail increases as we proceed outboard, and the effect of the wing becomes invariant of the longitudinal coordinate. From the figure it appears that the downwash on the high tail is smaller than that on the low one.

The effect of the near tail is also computed for a Mach number of 0.88 and zero angle of attack. Only high tails are considered in this case. Figure 5 shows the effect of the tail deflection upon the wing pressure distribution at two span stations. In the absence of the tail and for zero angle of attack the pressure distribution on the wing is symmetrical. Therefore, the differences between the curves at each span station reflect the effect of the presence of the tail upon wing surface pressures. The effect of the tail on the wing lower surface pressure is subtle (compare with the wing pressure distribution of Fig. 2 for the case of a tail situated at a distance of 0.12 the wing root chord downstream of the

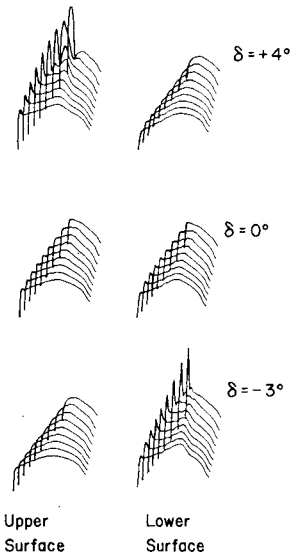

Fig. 6 Tail surface pressure distributions for different deflections ($M_\infty = 0.88$ and $\alpha = 0$ deg).

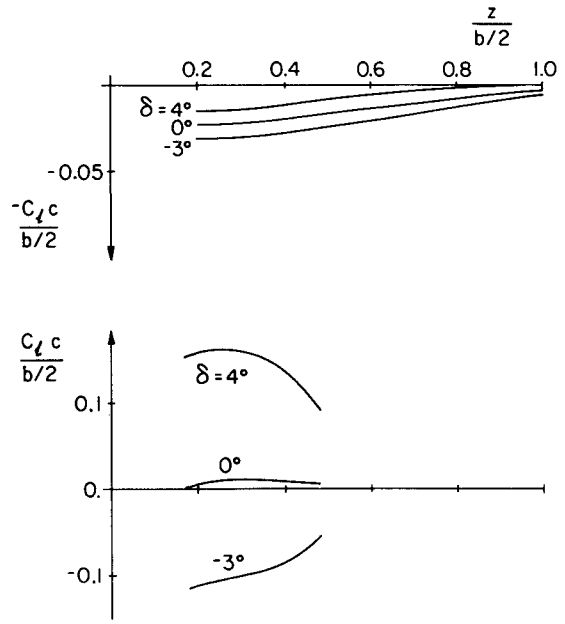

Fig. 7 Spanwise loadings on wing and tail as a function of tail deflection. Freestream Mach number 0.88 and zero angle of attack.

wing). The primary effect is due to blockage which causes a weakening of the aft shock on the upper surface of the wing.

Figure 6 shows the tail surface pressure distributions for the various tail deflections. The spanwise wing and tail loadings for these tails deflections are presented in Fig. 7. The load characteristics for both lifting surfaces are similar to those for the preceding freestream condition (see Fig. 4).

Finally, to examine the range of the various effects the tail has upon the wing, the wing lift is plotted as function of stagger in Fig. 8. The freestream Mach number is 0.88, the angle of attack is zero, and the tail is deflected to +4 deg. For very narrow gaps, the blockage effect of the tail causes a reduction in wing lift (which would be zero in the absence of the tail). This effect of the tail gradually subsides as the tail is moved further from the wing. At a gap of about one-half the wing chord, a different type of interaction takes over; at these greater distances the lifting surfaces may be considered as systems of line vortices which induce velocities upon each other. Thus at wide enough gaps, when the local blockage effect dwindles, the numerical results indicate an increase in lift relative to the tail-off situation.

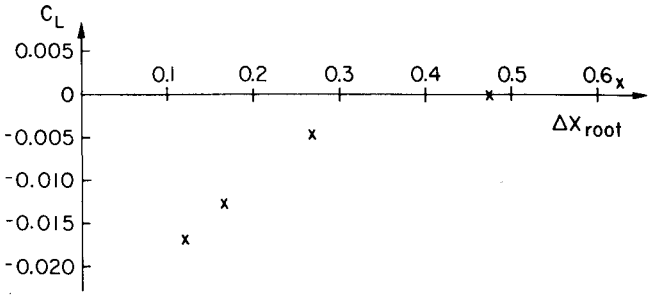

Fig. 8 Variation of wing lift due to the tail as a function of stagger.

Conclusions

A computer program for calculating the transonic potential flow past three-dimensional, wing-tail-fuselage configurations has been developed. In order to satisfy the boundary conditions at solid surfaces accurately, the difference equations are solved in a body-fitted mesh system. The computation is based upon a finite volume formulation, which uses only local properties of the mesh system. The incorporation of the tail requires that the computation be done on a slotted domain, but the computational labor required per mesh point is still only about 10% greater than that for a simpler wing-body code.

The difference equations are solved using the multigrid method in conjunction with an alternating-direction successive line overrelaxation smoothing algorithm. This allows practical computations to be performed on the very large grids required to resolve the flow features in the vicinity of each of the aerodynamic components of these complex configurations.

The results show that the aerodynamic interference between the wing and tail flowfields changes character as the tail is moved from a close-coupled location to further downstream. For the near tail location, the interference of the tail upon the wing flowfield is dominated by the local blockage effect associated with the tail leading edge. For more distant locations, the effect of the tail upon the wing flowfield is dominated by the downwash associated with the tail vortex system.

Acknowledgment

This work has been supported in part by the Office of Naval Research under Contract N00014-77-C-0033.

References

[1]Shmilovich, A. and Caughey, D. A., "Grid Generation for Wing-Tail-Fuselage Configurations," *Journal of Aircraft*, Vol. 22, June 1985, pp. 467-472.

[2]Shmilovich, A. and Caughey, D. A., "Application of the Multigrid Method to Calculations of Transonic Potential Flow about Wing-Fuselage Combinations," *Journal of Computational Physics*, Vol. 48, 1982, pp. 362-484.

[3]Caughey, D. A. and Shmilovich, A., "Multigrid Calculation of Transonic Potential Flows," *Numerical Methods in Fluids: Advances in Computational Transonics*, Vol. 4, edited by W. W. Habashi, Pineridge Press, Swansea, U.K., 1984.

[4]Caughey, D. A., "Multigrid Calculation of Three-Dimensional Transonic Potential Flows," *Applied Mathematics and Computation*, Vol. 13, 1983, pp. 241-260.

[5]Shmilovich, A., "Calculation of Transonic Potential Flow past Wing-Tail-Fuselage Configurations Using the Multigrid Method," Ph.D. Thesis, Cornell University, Ithaca, N.Y. 1983.

[6]Shmilovich, A. and Caughey, D. A., "A Program for Computing Transonic, Potential Flow past Wing-Tail-Fuselage Configurations," Sibley School of Mechanical and Aerospace Engineering, Cornell University, Ithaca, N.Y., Fluid Dynamics and Aerodynamics Rept. FDA-83-08, 1983.

[7]Jameson, A. and Caughey, D. A., "A Finite-Volume Method for Transonic Potential Flow Calculations," *Proceedings of the AIAA 3rd Computational Fluid Dynamics Conference*, Albuquerque, N.M., 1977, pp. 35-54.